Direct Visualization of Grain Boundaries in 2D Monolayer WS$_2$ via Induced Growth of CdS Nanoparticle Chains

Changyong Lan, Dapan Li, Ziyao Zhou, SenPo Yip, Heng Zhang, Lei Shu, Renjie Wei, Ruoting Dong, and Johnny C. Ho*

To date, wafer-scale synthesis of two-dimensional (2D) materials are well achieved by chemical vapor deposition, but the obtained monolayers typically have multidomains with electrical and optoelectronic properties affected by grain boundaries and domain sizes. When these 2D materials are used as the growth templates, these boundaries would also provide unknown influences to the successive heterostructure formation for extended applications. Here, for the first time, direct visualization of grain boundaries in monolayer WS$_2$ film can be realized by the growth of CdS nanoparticles. Specifically, CdS is found to first preferentially nucleate and form as nanoparticle chains along WS$_2$ grain boundaries in a random manner, independent of the grain boundary characteristics. Due to electron scattering and type II band alignment at the WS$_2$–CdS heterojunction, WS$_2$ reduces in its mobility while becoming enhanced in its electron concentration. Notably, the WS$_2$–CdS heterostructure also yields improved carrier separation and collection for the photodetection performance enhancement. All these results can facilitate the detailed evaluation of crystalline grains-related information of 2D materials and provide thorough understanding on the effect of these overgrown CdS on underlying WS$_2$ monolayers, being extremely important to further optimize and enable their functionalities for advanced device applications.

1. Introduction

Since the discovery of graphene in 2004, because of the atomically thin characteristics and the unique physical and chemical properties, two-dimensional (2D) materials have attracted tremendous attention in the scientific community.[1–5] To date, various kinds of 2D materials have been explored as superconductors, semimetals, semiconductors, topological insulators, and many others for next-generation electronics and optoelectronics.[6–8] Moreover, forming heterostructures from dissimilar 2D materials with different bandgaps and work functions can further enable and manipulate their novel properties. As there are only weak van der Waals interactions in the out-of-plane direction, there would not be any issue on the lattice registration when a 2D material is placed on top of another 2D material, making the formation of heterostructures with atomically sharp interfaces straightforward as compared with the conventional bulk materials.[9–11] In this case, simply by mechanically stacking multiple exfoliated 2D materials together, different transistor architectures can be readily achieved with the impressive device characteristics. For example, Georgiou et al. have fabricated high-performance graphene–WS$_2$–graphene heterostructure vertical field-effect transistors employing the stacking method;[12] however, the obtained heterostructure interface quality is still not satisfactory because numerous defects always exist at the interface and crystal orientations between the two layers are random.

In order to get the high-quality 2D heterostructures, chemical vapor deposition (CVD) is often utilized. Generally, 2D materials can serve as ideal templates for the growth of nanoplates, other 2D materials or even bulk materials via van der Waals epitaxy. By using CVD method, graphene–Bi$_2$Te$_3$,[13] graphene–MoS$_2$,[14] graphene–WS$_2$,[15] MoS$_2$–WS$_2$,[16,17] and MoS$_2$–CdS[18] vertical heterojunctions have been successfully synthesized. It is found that the quality of underlying 2D material templates is actually very important, dictating the growth of crystalline top materials. Since CVD grown 2D materials are usually polycrystalline with lots of defects[19–21] and these defects are mostly existed along the grain boundaries instead of locating within the in-domain area, these 2D

Dr. C. Lan, D. Li, Z. Zhou, S. P. Yip, H. Zhang, L. Shu, R. Wei, R. Dong, Prof. J. C. Ho
Department of Materials Science and Engineering
City University of Hong Kong
Hong Kong 999077, China
E-mail: johnnyho@cityu.edu.hk
Dr. C. Lan
School of Optoelectronic Science and Engineering
University of Electronic Science and Technology of China
Chengdu 610054, China
D. Li, Z. Zhou, S. P. Yip, H. Zhang, L. Shu, R. Wei, Prof. J. C. Ho
Shenzhen Research Institute
City University of Hong Kong
Shenzhen 518057, China
S. P. Yip, L. Shu, Prof. J. C. Ho
State Key Laboratory of Millimeter Waves
City University of Hong Kong
Hong Kong 999077, China
Prof. J. C. Ho
Centre for Functional Photonics
City University of Hong Kong
Hong Kong 999077, China

The ORCID identification number(s) for the author(s) of this article can be found under https://doi.org/10.1002/smtd.201800245.
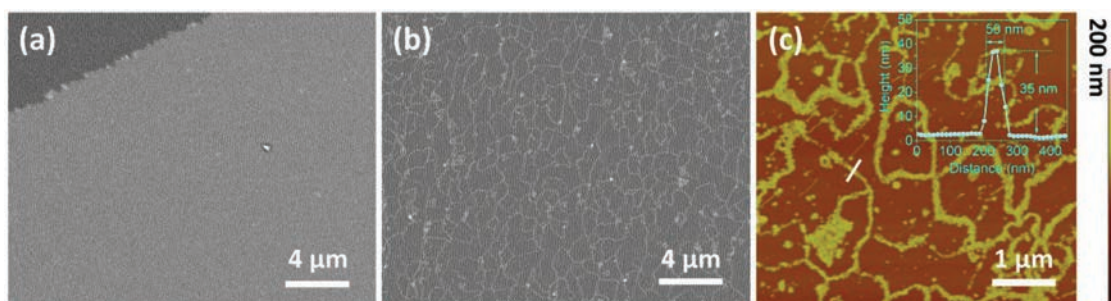
Figure 1. Morphology characterization of the obtained WS$_2$–CdS heterostructure. a) SEM image of the CVD grown WS$_2$ monolayer. The scratch was intentionally made on the upper left corner for the clear observation. b) SEM image of the grown WS$_2$–CdS heterostructure. c) AFM image of the CVD grown WS$_2$–CdS heterostructure. Inset shows the height profile tracing along the nanoparticle chain.

templates would drastically deteriorate the growth behavior of top materials. It is noted that these defects sites also have the high chemical activity, in which they have been exploited for the grain boundary visualization through oxidization.[22–24] In this respect, during the CVD growth of these heterojunctions, those defects typically provide low energy sites for the growth nucleation. It is therefore essential to assess this defects-related mechanistic growth of the top materials over the 2D templates. More importantly, it is also critical to evaluate the effect of this heterostructure formation on electrical and optoelectronic properties of the underlying 2D materials. All these would provide valuable insights into the realization of high-quality CVD heterostructures for their advanced utilizations.

Here, for the first time, we report the direct visualization of grain boundaries in 2D layer structured materials (i.e., CVD monolayer WS$_2$) without using any advanced sophisticated imaging techniques as well as propose and validate the mechanistic growth model for subsequent CdS–WS$_2$ heterostructure formation. It is observed that the CdS material would first preferentially form as nanoparticles along the WS$_2$ grain boundaries in a random manner independent of the grain boundary characteristics. In specific, based on the classical nucleation theory, owing to the existence of large quantities of defects at the WS$_2$ grain boundaries, CdS species are witnessed to be more easily adsorbed on these low energy boundaries rather than the in-plane area, which leads to the nucleation of CdS nanoparticles along the WS$_2$ grain boundaries. More importantly, due to electron scattering at the heterojunction, the electron mobility of WS$_2$ gets reduced after the overgrowth of CdS nanoparticle chains. On the other hand, attributed to the internal field established between CdS and WS$_2$ (i.e., type II band alignment), electrons would donate from CdS to WS$_2$ enhancing the electron density via n-doping. These heterostructures can also yield the impressively higher carrier separation and collection for the photogenerated electron–hole pairs, leading to the improved photodetection performance when configured into simple photodetectors. All these results can evidently reveal the mechanistic overgrowth of CdS along WS$_2$ grain boundaries, which provide thorough understanding on the effect of these overgrown CdS on the underlying WS$_2$ monolayers, being extremely important to further optimize their electrical and optoelectronic properties for advanced device applications.

2. Results and Discussion

In this work, utilizing our previously developed technique,[19] the pristine CVD grown monolayer WS$_2$ film has a relatively smooth surface (**Figure 1**a). After a short duration of the CVD overgrowth of CdS (i.e., 10 min), there is not any obvious change on the growth substrate as observed by the naked eye. However, based on the scanning electron microscopy (SEM) measurement, the substrate surface is modified significantly with a network-like morphology clearly witnessed (Figure 1b). This network-like morphology is also undoubtedly confirmed by atomic force microscopy (AFM) (Figure 1c). It can be clearly seen that the network lines are typically composed of the CdS nanoparticle chains. The corresponding height profile (across the white line) is shown in the inset of Figure 1c with the line width and height of ≈50 and ≈35 nm, respectively. Since this network-like morphology is found similar to the distribution of multidomains in a polycrystalline monolayer 2D film,[25] it is reasonable to hypothesize the CdS nanoparticles predominately growing along the grain boundaries of monolayer WS$_2$ such that each single crystalline WS$_2$ domain becomes visible under SEM. Notably, this hypothesis can be partly validated by the optical microscopy studies of fabricated WS$_2$–CdS heterostructures, where the exact same network morphology is also clearly observed after the overgrowth of CdS on WS$_2$ monolayers particularly with the larger single crystalline domain size (i.e., ≈10 µm) and transferred onto the Si/SiO$_2$ (270 nm) substrates (Figure S1, Supporting Information).

In order to further confirm the hypothesis, systematic transmission electron microscopy (TEM) measurement is then carried out. As illustrated in the typical TEM image of fabricated WS$_2$–CdS heterostructures (**Figure 2**a), it is obvious that the network lines are composed of CdS nanoparticles, being perfectly consistent with the AFM result. In particular, the average size of these CdS nanoparticles is about 20 nm, while they can also be seen along the edges of multilayer WS$_2$ domains (Figure S2, Supporting Information). The chemical composition of the CdS nanoparticles and the underlying WS$_2$ film are ascertained by energy dispersive X-ray spectroscopy (EDS) (Figure S3, Supporting Information). Generally, for 2D materials, the adjacent single crystalline domains have different crystal orientations, which can be used to identify different single crystalline domains.[26] This way, selected area electron diffraction (SAED) measurements are performed to evaluate the
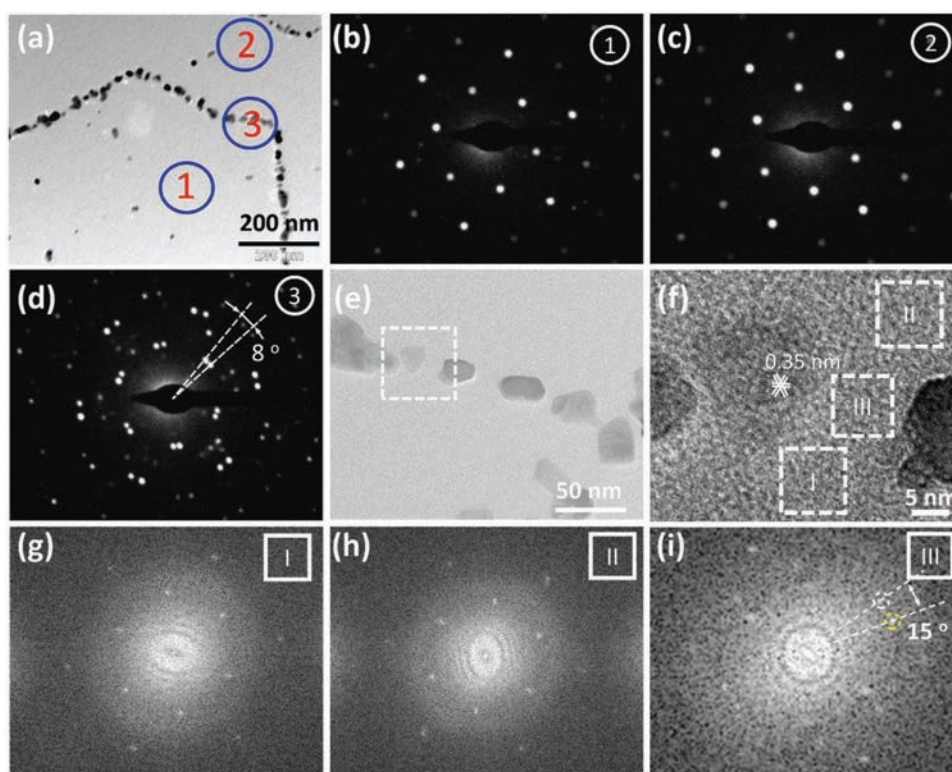
ADVANCED
SCIENCE NEWS
www.advancedsciencenews.com

small
methods
www.small-methods.com

Figure 2. TEM characterization of the obtained WS$_2$–CdS heterostructure. a) TEM image. b–d) SAED patterns of the labeled regions in the panel (a). e) High-magnification TEM image. f) HRTEM image of the labeled region in (e). g–i) FFT patterns of the labeled region in (f).

crystal orientation of the CdS nanoparticle chain as well as the both sides of WS$_2$ film separating by the nanoparticle chain. As depicted in Figure 2b,c, the regions 1 and 2 show only one set of diffraction spots corresponding to the single crystalline WS$_2$ with the zoom axis of [001], which indicates the single crystallinity of each area. However, the crystal orientation of these two areas is different since two sets of diffraction spots are observed in the SAED pattern obtained from region 3 (Figure 2d), belonging to the regions 1 and 2. It is also noted that the angle between these two sets of diffraction spots is about 8°, suggesting a misorientation of 8° at the domain boundary there. Apart from the diffraction spots from WS$_2$, some irregular spots are also observed, which belongs to CdS nanoparticles, designating the nanoparticle chains indeed located along the WS$_2$ grain boundaries. Next, high-resolution TEM (HRTEM) studies are as well performed to investigate the structural quality of fabricated WS$_2$–CdS heterostructures. Figure 2e,f presents the high-magnification TEM and HRTEM images along the chain region. Specifically, distinctive lattice fringes with a lattice spacing of 0.35 nm are observed for the CdS nanoparticles, which corresponds to {110} planes of the wurtzite CdS phase. Weak lattice fringes are also seen for the WS$_2$ film. To further confirm the different crystal orientations of the two sides of WS$_2$ separating by the CdS nanoparticle chain, fast Fourier transformation (FFT) are made accordingly. The FFT of both region I and II give the same hexagonal diffraction pattern with different orientations, which affirm the different crystal orientations of the two regions. Similarly, the FFT of the intersection region (region III) shows again the two sets of diffraction spots

with an angle of about 15°. All these results clearly suggest that the CdS nanoparticles preferentially grow along the WS$_2$ grain boundaries. Also, FFTs, which contain both the area of CdS and WS$_2$, are made to study the crystal orientation relationship between CdS and WS$_2$ as shown in Figure S4 of the Supporting Information. In explicit, the in-plane faces of the CdS nanoparticles are mostly (001) planes as indicated by the hexagonal diffraction spots with the [001] zone axis. However, CdS nanoparticles does not exhibit the van der Waals epitaxial relationship with WS$_2$ on both sides of the boundary as typically observed in van der Waals heterostructures. As a result, there is not any preferential orientation for the induced overgrowth of CdS nanoparticles on the WS$_2$ grain boundaries. This random orientation between the CdS nanoparticles and the WS$_2$ monolayers suggests their weak interactions at the growth interface due to the nearly perfect surface away from the boundaries.

To shed light assessing the growth behavior of CdS on monolayer WS$_2$, the deposition time dependent morphology evolution of fabricated WS$_2$–CdS heterostructures are carefully evaluated. **Figure 3**a–d traces along the corresponding morphology evolution upon the different deposition times of CdS. It is clear that CdS nanoparticles are first preferentially nucleated at the WS$_2$ grain boundaries and these nanoparticles would gradually converge into the network-like morphology. Figure 3e,f depicts the AFM images of those heterostructures with the specific CdS deposition time of 4 and 10 min, respectively. The obtained AFM morphologies agree very well with the SEM results. For the short deposition time (e.g., 4 min), majority of the nucleated CdS nanoparticles are aggregated
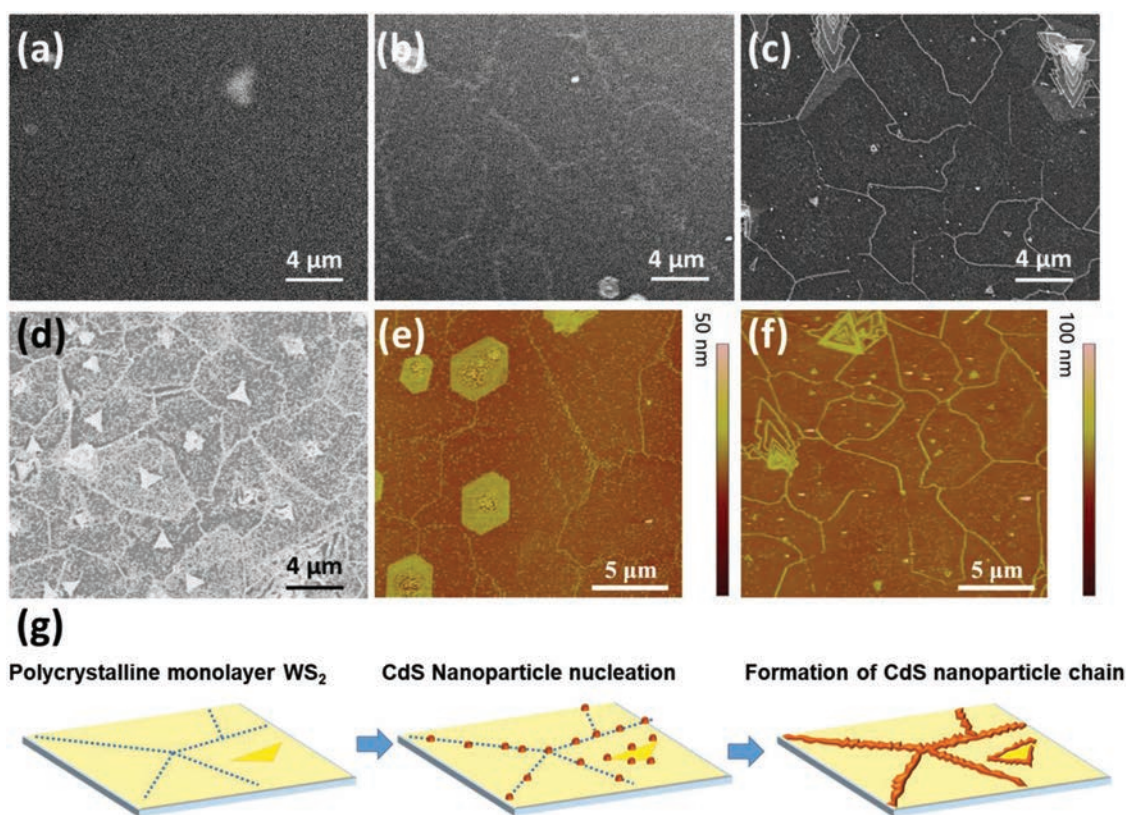
Figure 3. Morphology evolution and proposed mechanistic growth model of the obtained WS_2–CdS heterostructure. Morphology evolution as a function of the CdS deposition time. a) As prepared, SEM image. b) 4 min, SEM image. c) 10 min, SEM image. d) 60 min, SEM image. e) 4 min, AFM image. f) 10 min, AFM image. g) Schematic illustration of the proposed growth mechanism of CdS on WS_2. The light and dark yellow areas stand for the single and multilayer WS_2 domains, respectively. The blue dotted lines represent the WS_2 gain boundaries while the brown dots designate the CdS nanomaterials.

along the WS_2 grain boundaries in a relatively random manner without significant dependence on the grain boundary characteristics, such as the grain boundary angle, thickness, etc. For the long deposition time (e.g., 10 min), the WS_2 grain boundaries become more visible owing to the continuous growth of CdS nanoparticles along the boundaries. At the same time, an insignificant amount of CdS nanoparticles is still nucleated at the inner side of single crystalline domains because of the existence of few minor defects there. If an ultra-long deposition time (e.g., 60 min) is used, the growth of CdS nanoparticles would start to lose the preferential directionality, slowly to converge into continuous films (Figure 3d). Similar phenomenon can also be witnessed in the monolayer WS_2 with the smaller grain size of ≈0.8 µm (Figure S5, Supporting Information).

Based on the classical nucleation theory, in order to enrich our understanding in the growth characteristics of these heterostructures, the nucleation probability of CdS on the CVD synthesized monolayer WS_2 is investigated. At the WS_2 grain boundaries, there are always a large amount of defects, including sulfur and tungsten vacancies; therefore, there are lots of dangling bonds located at the boundaries. By contrast, there are very few dangling bonds existed within the single crystalline WS_2 domains due to their layered van der Waals crystal structure. As the enthalpic contribution to the free energy comes primarily from chemical bonding, the stronger

bonds would lead to the smaller interfacial free energy.[27] The small interfacial free energy means that the nucleation barrier height (E_B) is tiny as compared with that within a domain. This way, the nucleation probability at grain boundaries is high and CdS tends to nucleate at the grain boundaries accordingly. After nucleation, the continuous growth of CdS nuclei would highly depend on the surface migration of CdS species. Due to the existence of numerous dangling bonds near the CdS nuclei, the CdS species at nuclei would eventually have a slower migration rate as compared with those within the single domains.[28,29] As a result, the CdS nuclei will grow into nanoparticle chains at the WS_2 grain boundaries as schematically illustrated in the mechanistic growth model in Figure 3g. It should also be pointed out that as there are few defects existed within the single WS_2 domains, CdS would also get nucleated and grow into nanoparticles there, which is observed in the SEM, AFM, and TEM images.

In addition, various spectra characterization methods are also employed to further evaluate the physical and chemical properties of obtained WS_2–CdS heterostructures in detail. The following discussions are mostly based on the structures fabricated with WS_2 containing the large grain size of ≈10 µm and CdS deposition time of 10 min. **Figure 4**a demonstrates the optical absorption spectra of pristine monolayer WS_2 and WS_2–CdS heterostructure. It is obvious that the absorption
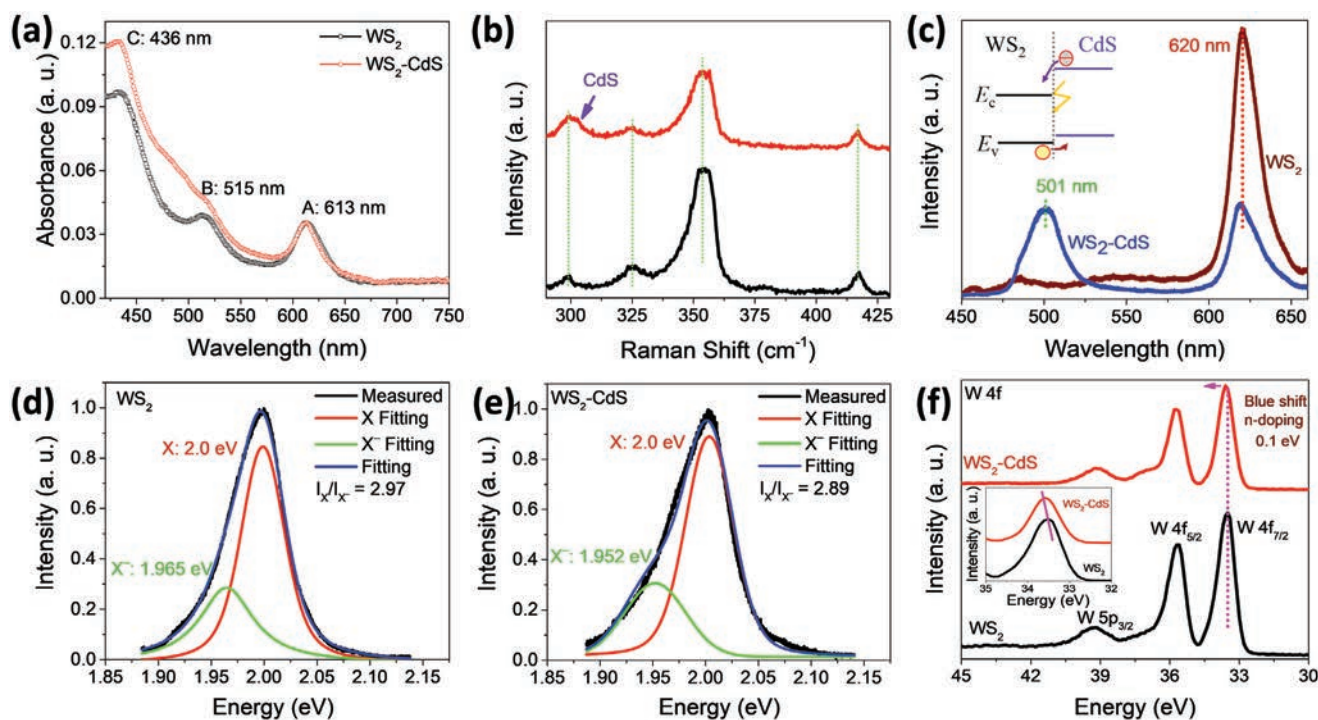
Figure 4. Spectra characterization of the obtained monolayer WS$_2$ and WS$_2$–CdS heterostructure. a) Optical absorption spectra. b) Raman spectra excited by a 532 nm laser. The peak associating with CdS is pointed out by a purple arrow. The peaks belonging to WS$_2$ are indicated by the dashed green line. c) PL spectrum excited by a 405 nm laser. Inset: Band alignment of the WS$_2$–CdS heterostructure. d,e) PL peak fittings for monolayer WS$_2$ and WS$_2$–CdS heterostructure. f) XPS of W 4f peak. Inset: Enlarged part of W $4f_{7/2}$ peak illustrating the blue-shift of the peak after heterostructure formation.

of WS$_2$–CdS heterostructure gets significantly improved at short wavelengths as compared with that of pristine WS$_2$, in which this enhancement can be attributed to the absorption of CdS nanoparticles.[30] As depicted in Figure 4b, Raman spectra are then collected to assess the chemical bonding information of the structures. In contrast to the Raman spectrum of monolayer WS$_2$, a new peak near 301 cm^{-1} is clearly observed, attributable to the 1-LO mode of CdS.[31] Since both CdS and monolayer WS$_2$ are direct bandgap semiconductors, photoluminescence (PL) spectra of monolayer WS$_2$ and WS$_2$–CdS heterostructure can be readily measured as shown in Figure 4c. Specifically, monolayer WS$_2$ yields a strong excitonic emission centered at 620 nm.[32] For WS$_2$–CdS heterostructure, the emission from WS$_2$ is reduced and a new emission peak near 501 nm is observed. The 501 nm emission can be ascribed to the bandgap related emission of CdS.[31] As the excitonic emission profile of WS$_2$ is strongly related to the carrier density in WS$_2$,[33] the emission peak from WS$_2$ can then be deconvoluted into two peaks originated from exciton (X) and trion (X$^-$) as given in Figure 4d,e. It is explicit that the peak position of X shows almost no shift, while the peak position X$^-$ exhibits a red shift after the deposition of CdS. The emission intensity ratio of X and X$^-$ also get reduced after the CdS deposition. These peak shift and peak intensity ratio (X/X$^-$) reduction suggest that there is an enhanced electron density of WS$_2$ constituted in the WS$_2$–CdS heterostructures.[33] Based on the band alignment of the WS$_2$–CdS heterostructure (Figure 4c, inset), CdS would donate electrons (i.e., n-doping) into WS$_2$ due to the type II band alignment, which leads to an increased electron

density in WS$_2$. This n-type doping can also be confirmed by X-ray photoelectron spectroscopy (XPS) as shown in Figure 4f. The W 4f peaks yield a blue shift of 0.1 eV after the CdS deposition (Figure 4f, inset), indicating the n-doping behavior in the underlying monolayer WS$_2$.[34] All these experimental findings evidently illustrate the profound effect of WS$_2$–CdS heterostructure formation on the optical absorption and carrier density modulation of 2D WS$_2$ materials.

Apart from the carrier density modulation, the carrier transport properties of WS$_2$ may also be affected by the formation of WS$_2$–CdS heterostructure. In this case, field-effect transistors (FETs) based on monolayer WS$_2$ and WS$_2$–CdS heterostructure are fabricated and thoroughly characterized. **Figure 5**a,b shows the representative output characteristics of fabricated devices, while the figure insets give the SEM images of devices configured in the global back-gate geometry accordingly. In specific, both types of the devices exhibit typical n-type conducting behaviors as the source–drain current, I_{ds}, increases with the increasing gate voltage, V_{gs}. Considering the same transistor dimension, as depicted in the device transfer characteristics in Figure 5c, the gate coupling of monolayer WS$_2$ FET is more efficient due to the observation of a larger ON-current as compared to the one of WS$_2$–CdS heterostructure FET. Inevitably, both devices display the large hysteresis, which is probably ascribed to the defects, moveable charged ions on gate dielectric (i.e., SiO$_2$), adsorbed molecules, interface traps, etc. along the device channel surface.[35–37] In fact, the difference of threshold voltage (ΔV_{th}) between the forward and the backward gate voltage sweeping is always used as a parameter
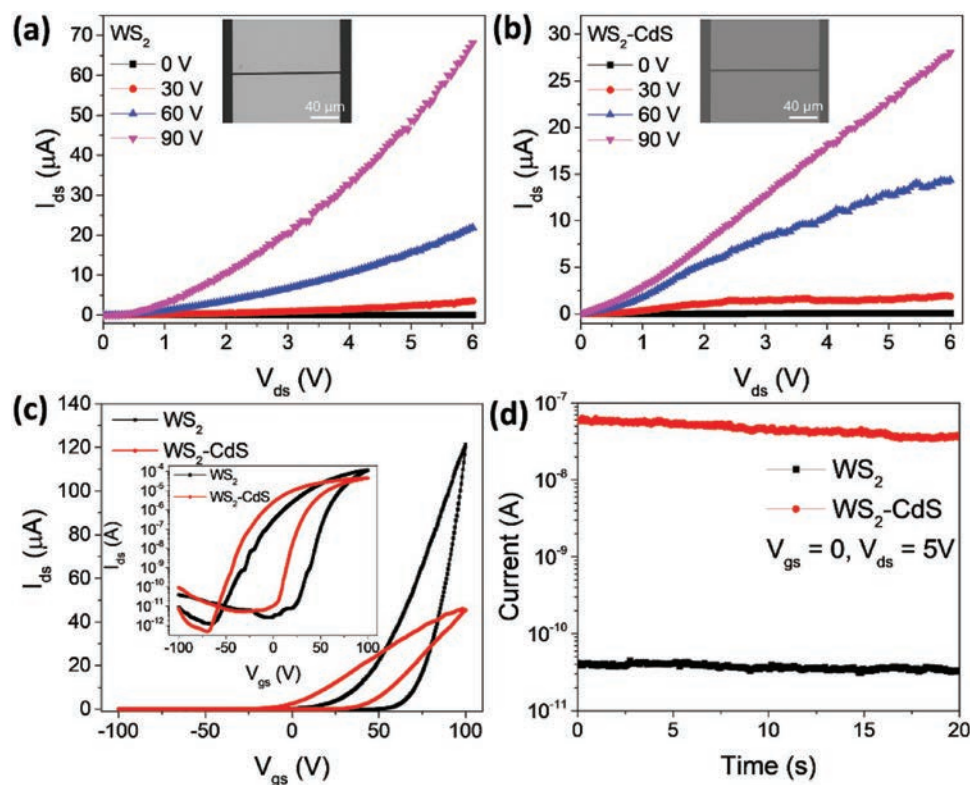
ADVANCED
SCIENCE NEWS
www.advancedsciencenews.com

small
methods
www.small-methods.com

Figure 5. Electronic transport properties of the fabricated WS_2 and WS_2–CdS heterostructure FETs. Output characteristics of a) WS_2 FET. b) WS_2–CdS FET. c) Transfer characteristics of WS_2 and WS_2–CdS FETs with V_{ds} = 5 V. d) Source–drain current as a function of time. The inset in (a) and (b) give the representative SEM images of the corresponding devices.

evaluating the hysteresis phenomenon. Here, the ΔV_{th} is 33 V for the typical WS_2 based transistor while it increases to 45 V for the WS_2–CdS heterostructure based transistor. In this case, the trapping of charges induced by defects, adsorbents, etc. is the origin of hysteresis observed in the transfer curve. More defects are thought to be introduced after the growth of CdS nanoparticles, which might be the reason for the enlarged hysteresis in WS_2–CdS heterostructure based transistors. In any case, both devices yield a remarkably high ON/OFF current ratio of $\approx 10^8$. The field-effect mobility of the device channel can also be calculated using the following formula of

$$\mu = \frac{\partial I_{ds}}{\partial V_{gs}} \cdot \frac{L}{W} \cdot \frac{1}{C_{ox} V_{ds}} \qquad (1)$$

where L is the channel length, W is the channel width, C_{ox} is the gate capacitance per unit area, and V_{ds} is the source–drain voltage. In this work, the mobility of the monolayer WS_2 is found to be 0.74 cm^2 V^{-1} s^{-1}, while the mobility of WS_2–CdS heterostructure is determined to be 0.14 cm^2 V^{-1} s^{-1}. In fact, we have measured more than 10 devices for each sample group of monolayer WS_2 and WS_2–CdS heterostructure FETs, where the average mobility is measured to be 0.81 and 0.11 cm^2 V^{-1} s^{-1}, respectively. This way, the channel mobility gets reduced after the deposition of CdS nanoparticles. The reduced mobility can be attributed to the electron scattering by CdS nanoparticles since the CdS nanoparticles located along the WS_2 grain boundaries would act as the ionic scattering centers due to the

type II band alignment. The electron transfer phenomenon (from CdS to WS_2) can again be experimentally confirmed by the time dependent current response (I_{ds} vs t) of the devices (Figure 5d). Obviously, the WS_2–CdS device has a larger output current as compared with that of WS_2 device, indicating the n-type doping in WS_2 constituted in the WS_2–CdS heterostructure. It is apparent that as a result of electron scattering at the heterojunction, the electron mobility of WS_2 would get substantially degraded after the overgrowth of CdS nanoparticle chains.

As both WS_2 and CdS are good optoelectronic materials, which have wide applications in optoelectronics, it is critical to investigate their photosensing properties of the fabricated devices. Here, photodetectors based on monolayer WS_2 and WS_2–CdS heterostructure are configured using interdigital Au electrodes as shown in the inset of **Figure 6**a,b. From the current–voltage (I–V) curves with and without light illumination using a 450 nm laser as the light source (Figure 6a,b), both devices are very sensitive to the incident light, where the output current increases with the increasing light intensity. Considering the same light intensity and device dimension, the output current of WS_2–CdS heterostructure photodetector is found to be much larger as compared with the one of monolayer WS_2, suggesting that the deposition of CdS nanoparticles can substantially enhance the photodetection performance of WS_2. In general, photocurrent, I_p, is always defined as the difference of the current with and without light illumination. This way, the photocurrent as a function of light intensity of
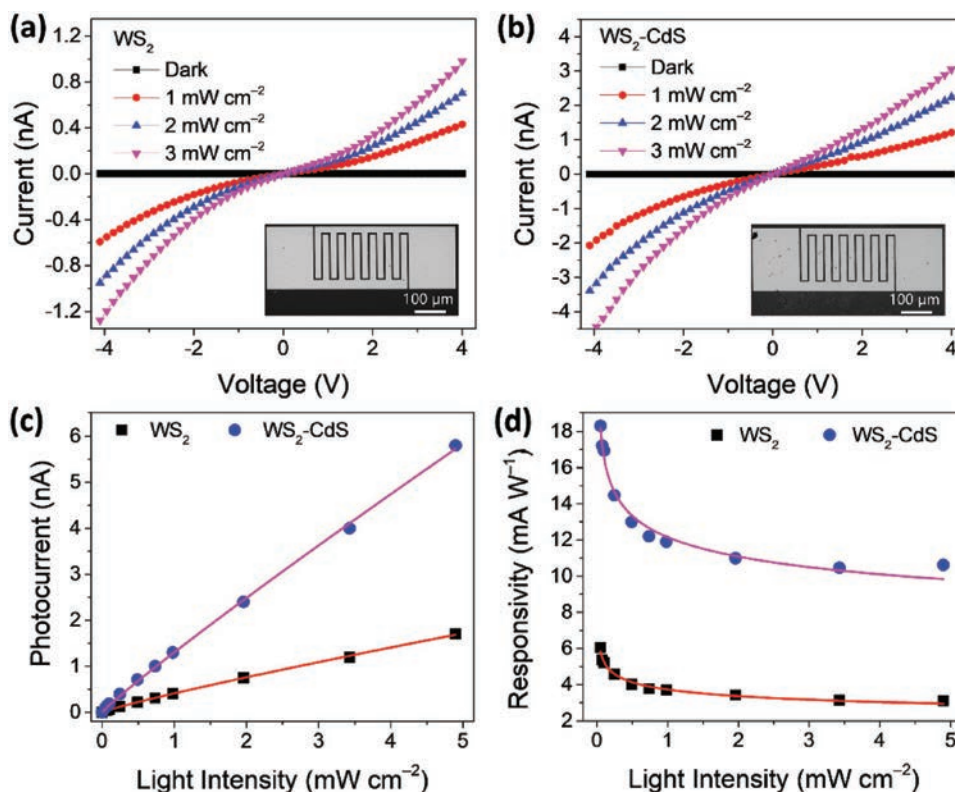
Figure 6. Photodetection characteristics of the fabricated WS$_2$ and WS$_2$–CdS heterostructure devices measured with a 450 nm laser as light source. I–V curves of a) monolayer WS$_2$ and b) WS$_2$–CdS heterostructures based photodetectors with and without light illumination. c) Photocurrent versus light intensity. d) Responsivity versus light intensity. The bias voltage is 4 V for (c) and (d). The inset in (a) and (b) give the SEM images of the corresponding devices.

both devices are also measured (Figure 6c). The increasing trend of photocurrent with the increasing light intensity is perfectly consistent with the I–V curves. From the photocurrent curves, it is clear that the WS$_2$–CdS heterostructure is more photosensitive to light than monolayer WS$_2$. Explicitly, the photocurrent of WS$_2$–CdS heterostructure based photodetector is about 3.4 times larger than that of monolayer WS$_2$ device when the light intensity is 4.9 mW cm^{-2}. Since the photocurrent has almost a linear relationship with light intensity for both devices, these relationships can be well fitted by the following expression of

$$I_p = A\Phi^\beta \tag{2}$$

where A and β is are fitting parameters and Φ is the light intensity. By fitting the data, β is found to be 0.89 and 0.93 for WS$_2$ and WS$_2$–CdS heterostructure based photodetectors, respectively. The sublinear behavior is a result of complex process of carrier generation, trapping, and recombination in the photosensing material, which is always observed in photoconductor devices.[38–40] As compared with the WS$_2$ device, the power factor (β) increases for the WS$_2$–CdS device. In fact, the value of β is closely related to the distribution of trap states within the forbidden gap. Usually, if the trap states have an exponential distribution of $N_t = N_0\exp(-(E_c - E)/kT_1)$, where N_0 is a constant, E_c is valance band level, E is the trap energy level, k is the Boltzmann constant, T_1 is a characteristic parameter

for the trap states distribution and $T_1 > T$ (T the ambient temperature), the photocurrent has a relationship of $I_p \propto \Phi^{\frac{T_1}{T_1+T}}$.[41] Therefore, when the β value is between 0.5 and 1, it is then highly depended on the distribution of traps, i.e., the value of T_1. This way, the increase of the β value after the deposition of CdS can be attributed to the redistribution of trap states with a more uniform distribution (e.g., larger T_1). At the same time, responsivity (R) is another figure-of-merit to illustrate the sensitivity of a photodetector, which is analytically defined as

$$R = \frac{I_p}{\Phi S} \tag{3}$$

where S active area of the photodetector. According to both Equations (2) and (3), R should be proportional to $\Phi^{\beta-1}$. This way, the responsivity would decrease with the increasing light intensity as shown in Figure 6d. The maximum responsivity is then determined as 6.0 and 18.3 mA W^{-1} under light intensity of 50 µW cm^{-2} for WS$_2$ and WS$_2$–CdS heterostructure, accordingly. Furthermore, the ability to detect weak signal is also important for a photodetector, which can be stand for by specific detectivity (D*) with the following expression
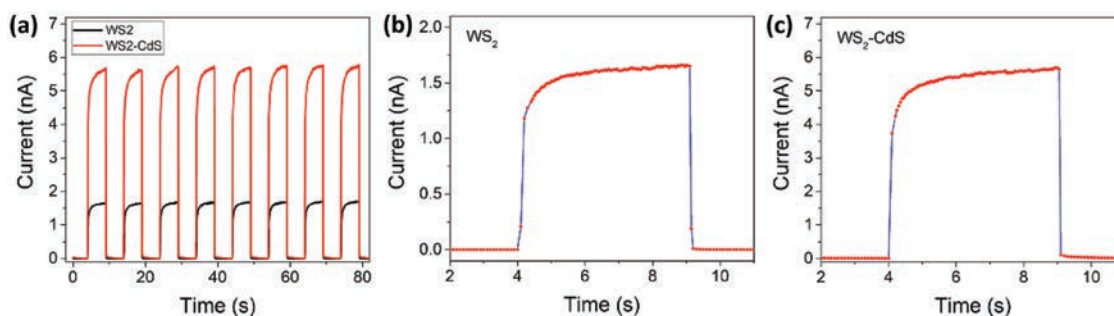
$$D^* = R\sqrt{\frac{S}{2qI_{dark}}} \tag{4}$$

ADVANCED
SCIENCE NEWS
www.advancedsciencenews.com

small
methods
www.small-methods.com

Figure 7. Transient properties of the WS_2 and WS_2–CdS heterostructure photodetectors. a) Current versus time response under modulated light illumination. Magnified part of the curve of b) WS_2 and c) WS_2–CdS heterostructure based photodetectors. The light intensity and bias voltage is 4.9 mW cm^{-2} and 4 V, respectively.

where I_{dark} is the dark current and q is the charge of an electron. Based on (4), $D*$ is proportional to R, thus it has the similar trend with the light intensity as shown in Figure S6 of the Supporting Information. The maximum specific detectivity is extracted to be 2.3×10^{11} Jones and 7.3×10^{11} Jones under light intensity of 50 μW cm^{-2} for WS_2 and WS_2–CdS heterostructures based photodetectors, respectively. All the obtained performance parameters are comparable or even better than some of the state-of-the-art 2D materials based photodetectors.[42–50] This photodetection performance enhancement after the CdS deposition on WS_2 can be attributed to the type II band alignment resulted from the formation of WS_2–CdS heterostructure (Figure 4c, inset). The photoexcited electron–hole pairs can then be separated by the internal electrical field established between CdS and WS_2 such that electrons would transfer to the WS_2 side while holes would move to the CdS side. As a result, the corresponding nonequilibrium carrier lifetime increases, leading to the increase of photogain, which is similar to the case observed in other heterostructure systems.

For practical applications, the transient response of a photodetector is also extremely important. As shown in **Figure 7**a, the output current of monolayer WS_2 and WS_2–CdS heterostructure photodetectors under modulated light illumination is carefully measured. Notably, clear ON and OFF states with the excellent stability of both devices is witnessed under modulated light illumination. In order to determine the response time of photodetectors, the magnified parts of the transient curves of monolayer WS_2 and WS_2–CdS heterostructure devices are shown in Figure 7b,c, respectively. In detail, both devices exhibit a fast rise followed by a slow increase of the current when the light is switched on. This "quick" part (i.e., fast rise) of the photocurrent change contributes to a response time of less than 50 ms, suggesting the remarkably fast response of our devices. The "slow" part (i.e., slow increase) of the photocurrent change can be attributed to the carrier traps existed on the device channel surface, in which photogenerated carriers would first fill the traps and then the photocurrent can reach the maximum after all traps are occupied, bringing a deferral to get to the steady photocurrent.[51] It is also worth to point out that there are not any slow decrease behaviors for both devices when the light is turned off, indicating the fast release of trapped charges there. All these results obviously demonstrate the photodetection performance enhancement of WS_2–CdS heterostructures

over monolayer WS_2, being promising for the next-generation advanced optoelectronics.

3. Conclusion

In conclusion, WS_2–CdS heterostructures have been successfully synthesized by CVD, where CdS materials are found to preferentially nucleate and form as nanoparticle chains along the WS_2 grain boundaries. By employing complementary characterization techniques, a mechanistic growth model for the WS_2–CdS heterostructure formation is proposed and validated based on the classical nucleation theory. Importantly, during the growth, the monolayer WS_2 grain boundaries can be directly visualized by simple imaging techniques, including optical microscope, without using any complicated procedures. At the same time, the formation of these WS_2–CdS heterostructures is also observed to strongly affect the corresponding optical, electrical and optoelectronic properties of the underlying WS_2 monolayer. All these results do not only provide a simple path to obtain crystalline grains related information of 2D materials, but also enable the tuning of their properties for their next-generation electronics and optoelectronics.

4. Experimental Section

Synthesis of Monolayer WS_2 Films: CVD was used for the synthesis of monolayer WS_2, which has been reported before.[19] Briefly, a three-zone horizontal tube furnace with a 1 in. diameter quartz tube was used as the heating device. WO_3 powders (200 mg) placed in a quartz boat was positioned in the center zone of the tube furnace. A sapphire substrate was located at the center of the right zone (downstream side). Sulfur powders (300 mg) placed in a ceramic boat was positioned out of the left zone (upstream side), which was heated by a heating belt. The left zone was intentionally unheated to make sure that the sulfur powder was heated with a controllable temperature. Before heating, the pressure inside the quartz tube was pumped down to 1 mTorr, and then 30 sccm high impurity (99.999%) argon was introduced into the tube as the carrier gas. The pressure was kept at 0.16 Torr during the deposition. The center zone and the right zone were heated to 920 and 900 °C, respectively. The deposition was kept for 40 min. After the deposition, the temperature was cooled down naturally. The grain size of the monolayer WS_2 film can be controlled by tuning the heating temperature of the sulfur. A low heating temperature (110 °C) would lead to the small single domain size. Large single domain size can be obtained with a

high heating temperature of sulfur (160 °C) even though the multilayer nucleation is also promoted at the same time.

Synthesis CdS Nanoparticles on Monolayer WS₂ Films: A single-zone furnace with a 1 in. diameter quartz tube was used for the synthesis. CdS powder (5 mg) placed in a quartz boat was positioned in the center of the furnace. WS₂ pregrown on sapphire was then placed in the downstream side of the quartz tube, which is 15 cm away from the center. The experiment was carried out in ambient pressure. Before heating, the quartz tube was flushed with Ar gas with a flow rate of 200 sccm. Then, the furnace was heated to 750 °C in 30 min and kept at that temperature for a duration of 4–60 min. After the synthesis, the furnace was cooled down to room temperature naturally.

Transfer of WS₂ and WS₂–CdS Heterostructure Films onto SiO₂/Si Substrates and Cu Grids: The transfer of WS₂ and WS₂–CdS heterostructures from the growth substrate to the required substrate is realized by utilizing surface energy assisted method.[52] Polystyrene (PS) solution (140 mg mL⁻¹ in toluene) was spin-coated onto WS₂/sapphire WS₂–CdS/sapphire samples with a rotating rate of 4000 rpm. After that, the samples were baked at 90 °C for 20 min on a hot plate. The sample was placed then in a glass garden and a drop of water was dropped on the top of the sample. The edge of the PS film was scribbled with a knife to facilitate the penetration of water molecules. Next, the PS/WS₂ or PS/WS₂–CdS film would separate from the sapphire substrate. Water was also added to the glass garden so that the film will float on the surface of water. SiO₂/Si substrates with the thermal oxide thickness of 270 nm or Cu grid was used to fish out the film. After drying in air, the sample was baked at 120 °C on a hot plate for 20 min. After that, the sample was dipped in toluene to dissolve the PS coating.

Characterization: SEM (G2 Pro, PhenomWorld) and AFM (diMultimode V, Veeco) were used to inspect the surface morphology of the films. The morphology of the samples was also checked by TEM (CM-20, Philips). SAED patterns were used to evaluate the crystal quality of the samples. HRTEM images were obtained from another TEM instrument (2100F, JEOL). EDS spectra were collected from the detector attached on CM-20 TEM instrument to analyze the chemical composition of the samples. Raman spectroscopy (SR-5001-A-R, Andor) was employed to obtain the Raman spectra (excited by a 532 nm laser) and PL spectra (excited by a 405 nm laser) of the samples. XPS (ULVAC-PHI5802) was used to get XPS spectra of the samples.

Device Fabrication and Measurements: For the fabrication of field-effect transistors and photodetectors, standard photolithography method was used to define the source and the drain regions, and 5 nm Ti and 50 nm Au were deposited successively by e-beam evaporation followed by a lift-off process. The electrical performance of field-effect transistors was measured in a vacuum probe station. Before measurements, the chamber was pumped for one day to confirm the high vacuum. The vacuum is 4×10^{-4} Pa during the measurements. The photodetector performance was measured in air with a standard electrical probe station. The active area of the photodetectors is 1.115×10^{-4} cm². An Agilent 4155C semiconductor analyzer was used as source and measurement unit. A 450 nm laser was used as the light source for photodetector measurement. The light was conducted to the probe station by a fiber with a collimator. A homemade electrically controlled mechanical shutter was used to modulate the incident light. The light intensity was tuned by an attenuator and measured by an optical power meter (PM400, Thorlabs).

Supporting Information

Supporting Information is available from the Wiley Online Library or from the author.

Acknowledgements

Conflict of Interest

The authors declare no conflict of interest.

Keywords

[1] G. R. Bhimanapati, Z. Lin, V. Meunier, Y. Jung, J. Cha, S. Das, D. Xiao, Y. Son, M. S. Strano, V. R. Cooper, L. Liang, S. G. Louie, E. Ringe, W. Zhou, S. S. Kim, R. R. Naik, B. G. Sumpter, H. Terrones, F. Xia, Y. Wang, J. Zhu, D. Akinwande, N. Alem, J. A. Schuller, R. E. Schaak, M. Terrones, J. A. Robinson, *ACS Nano* **2015**, *9*, 11509.

[2] M. Chhowalla, D. Jena, H. Zhang, *Nat. Rev. Mater.* **2016**, *1*, 16052.

[3] X. Duan, C. Wang, A. Pan, R. Yu, X. Duan, *Chem. Soc. Rev.* **2015**, *44*, 8859.

[4] C. Xie, C. Mak, X. Tao, F. Yan, *Adv. Funct. Mater.* **2017**, *27*, 1603886.

[5] S. Yang, W. Niu, A. L. Wang, Z. Fan, B. Chen, C. Tan, Q. Lu, H. Zhang, *Angew. Chem., Int. Ed.* **2017**, *56*, 4252.

[6] K. J. Koski, Y. Cui, *ACS Nano* **2013**, *7*, 3739.

[7] Q. H. Wang, K. Kalantar-Zadeh, A. Kis, J. N. Coleman, M. S. Strano, *Nat. Nanotechnol.* **2012**, *7*, 699.

[8] D. L. Duong, S. J. Yun, Y. H. Lee, *ACS Nano* **2017**, *11*, 11803.

[9] A. K. Geim, I. V. Grigorieva, *Nature* **2013**, *499*, 419.

[10] Y. Liu, N. O. Weiss, X. Duan, H.-C. Cheng, Y. Huang, X. Duan, *Nat. Rev. Mater.* **2016**, *1*, 16042.

[11] H. Lim, S. I. Yoon, G. Kim, A.-R. Jang, H. S. Shin, *Chem. Mater.* **2014**, *26*, 4891.

[12] T. Georgiou, R. Jalil, B. D. Belle, L. Britnell, R. V. Gorbachev, S. V. Morozov, Y.-J. Kim, A. Gholinia, S. J. Haigh, O. Makarovsky, L. Eaves, L. A. Ponomarenko, A. K. Geim, K. S. Novoselov, A. Mishchenko, *Nat. Nanotechnol.* **2013**, *8*, 100.

[13] H. Qiao, J. Yuan, Z. Xu, C. Chen, S. Lin, Y. Wang, J. Song, Y. Liu, Q. Khan, H. Y. Hoh, C.-X. Pan, S. Li, Q. Bao, *ACS Nano* **2015**, *9*, 1886.

[14] H. Ago, H. Endo, P. Solís-Fernández, R. Takizawa, Y. Ohta, Y. Fujita, K. Yamamoto, M. Tsuji, *ACS Appl. Mater. Interfaces* **2015**, *7*, 5265.

[15] C. Lan, C. Li, S. Wang, T. He, Z. Zhou, D. Wei, H. Guo, H. Yang, Y. Liu, *J. Mater. Chem. C* **2017**, *5*, 1494.

[16] Y. Gong, J. Lin, X. Wang, G. Shi, S. Lei, Z. Lin, X. Zou, G. Ye, R. Vajtai, B. I. Yakobson, H. Terrones, M. Terrones, B. K. Tay, J. Lou, S. T. Pantelides, Z. Liu, W. Zhou, P. M. Ajayan, *Nat. Mater.* **2014**, *13*, 1135.

[17] Y. Yu, S. Hu, L. Su, L. Huang, Y. Liu, Z. Jin, A. A. Purezky, D. B. Geohegan, K. W. Kim, Y. Zhang, L. Cao, *Nano Lett.* **2014**, *15*, 486.

[18] W. Zheng, W. Feng, X. Zhang, X. Chen, G. Liu, Y. Qiu, T. Hasan, P. Tan, P. A. Hu, *Adv. Funct. Mater.* **2016**, *26*, 2648.

[19] C. Lan, Z. Zhou, Z. Zhou, C. Li, L. Shu, L. Shen, D. Li, R. Dong, S. Yip, J. C. Ho, *Nano Res.* **2018**, *11*, 3371.

[20] Y. Yu, C. Li, Y. Liu, L. Su, Y. Zhang, L. Cao, *Sci. Rep.* **2013**, *3*, 1866.

[21] K. Kang, S. Xie, L. Huang, Y. Han, P. Y. Huang, K. F. Mak, C.-J. Kim, D. Muller, J. Park, *Nature* **2015**, *520*, 656.

[22] Y. Rong, K. He, M. Pacios, A. W. Robertson, H. Bhaskaran, J. H. Warner, *ACS Nano* **2015**, *9*, 3695.

[23] T. H. Ly, M.-H. Chiu, M.-Y. Li, J. Zhao, D. J. Perello, M. O. Cichocka, H. M. Oh, S. H. Chae, H. Y. Jeong, F. Yao, L.-J. Li, Y. H. Lee, *ACS Nano* **2014**, *8*, 11401.

[24] Y. Zhang, Y. Zhang, Q. Ji, J. Ju, H. Yuan, J. Shi, T. Gao, D. Ma, M. Liu, Y. Chen, X. Song, H. Y. Hwang, Y. Cui, Z. Liu, *ACS Nano* **2013**, *7*, 8963.

[25] X. Yin, Z. Ye, D. A. Chenet, Y. Ye, K. O'Brien, J. C. Hone, X. Zhang, *Science* **2014**, *344*, 488.

[26] K. Kim, Z. Lee, W. Regan, C. Kisielowski, M. Crommie, A. Zettl, *ACS Nano* **2011**, *5*, 2142.

[27] J. J. De Yoreo, P. G. Vekilov, *Rev. Mineral. Geochem.* **2003**, *54*, 57.

[28] L. Huang, Y. Yu, C. Li, L. Cao, *J. Phys. Chem. C* **2013**, *117*, 6469.

[29] *Physics of Crystal Growth* (Eds: A. Pimpinelli, J. Villain), Cambridge University Press, Cambridge **1998**.

[30] L. Qi, H. Cölfen, M. Antonietti, *Nano Lett.* **2001**, *1*, 61.

[31] T. Orii, S.-i. Kaito, K. Matsuishi, S. Onari, T. Arai, *J. Phys.: Condens. Matter* **2002**, *14*, 9743.

[32] W. Zhao, Z. Ghorannevis, L. Chu, M. Toh, C. Kloc, P.-H. Tan, G. Eda, *ACS Nano* **2012**, *7*, 791.

[33] J. Shang, X. Shen, C. Cong, N. Peimyoo, B. Cao, M. Eginligil, T. Yu, *ACS Nano* **2015**, *9*, 647.

[34] M. H. Chiu, W. H. Tseng, H. L. Tang, Y. H. Chang, C. H. Chen, W. T. Hsu, W. H. Chang, C. I. Wu, L. J. Li, *Adv. Funct. Mater.* **2017**, *27*, 1603756.

[35] W. Kim, A. Javey, O. Vermesh, Q. Wang, Y. Li, H. Dai, *Nano Lett.* **2003**, *3*, 193.

[36] T. Li, G. Du, B. Zhang, Z. Zeng, *Appl. Phys. Lett.* **2014**, *105*, 093107.

[37] Y. Park, H. W. Baac, J. Heo, G. Yoo, *Appl. Phys. Lett.* **2016**, *108*, 083102.

[38] Q. Li, T. Gao, T. Wang, *Appl. Phys. Lett.* **2005**, *86*, 193109.

[39] C. Lan, C. Li, Y. Yin, H. Guo, S. Wang, *J. Mater. Chem. C* **2015**, *3*, 8074.

[40] R.-S. Chen, H.-Y. Chen, C.-Y. Lu, K.-H. Chen, C.-P. Chen, L.-C. Chen, Y.-J. Yang, *Appl. Phys. Lett.* **2007**, *91*, 223106.

[41] *Photoelectronic Properties of Semiconductors* (Ed: R. H. Bube), Cambridge University Press, Cambridge, UK **1992**.

[42] Y. Xie, B. Zhang, S. Wang, D. Wang, A. Wang, Z. Wang, H. Yu, H. Zhang, Y. Chen, M. Zhao, B. Huang, L. Mei, J. Wang, *Adv. Mater.* **2017**, *29*, 1605972.

[43] J. Yao, Z. Zheng, J. Shao, G. Yang, *Nanoscale* **2015**, *7*, 14974.

[44] C. Lan, R. Dong, Z. Zhou, L. Shu, D. Li, S. Yip, J. C. Ho, *Adv. Mater.* **2017**, *29*, 1702759.

[45] H. Huang, J. Wang, W. Hu, L. Liao, P. Wang, X. Wang, F. Gong, Y. Chen, G. Wu, W. Luo, H. Shen, T. Lin, J. Sun, X. Meng, X. Chen, J. Chu, *Nanotechnology* **2016**, *27*, 445201.

[46] S. R. Tamalampudi, Y.-Y. Lu, R. Kumar U, R. Sankar, C.-D. Liao, K. Moorthy B, C.-H. Cheng, F. C. Chou, Y.-T. Chen, *Nano Lett.* **2014**, *14*, 2800.

[47] R. B. Jacobs-Gedrim, M. Shanmugam, N. Jain, C. A. Durcan, M. T. Murphy, T. M. Murray, R. J. Matyi, R. L. Moore, B. Yu, *ACS Nano* **2013**, *8*, 514.

[48] X. Zhou, Q. Zhang, L. Gan, H. Li, T. Zhai, *Adv. Funct. Mater.* **2016**, *26*, 4405.

[49] P. Hu, J. Zhang, M. Yoon, X.-F. Qiao, X. Zhang, W. Feng, P. Tan, W. Zheng, J. Liu, X. Wang, J. C. Idrobo, D. B. Geohegan, K. Xiao, *Nano Res.* **2014**, *7*, 694.

[50] W. Huang, L. Gan, H. Yang, N. Zhou, R. Wang, W. Wu, H. Li, Y. Ma, H. Zeng, T. Zhai, *Adv. Funct. Mater.* **2017**, *27*, 1702448.

[51] Y. Jiang, W. J. Zhang, J. S. Jie, X. M. Meng, X. Fan, S. T. Lee, *Adv. Funct. Mater.* **2007**, *17*, 1795.

[52] A. Gurarslan, Y. Yu, L. Su, Y. Yu, F. Suarez, S. Yao, Y. Zhu, M. Ozturk, Y. Zhang, L. Cao, *ACS Nano* **2014**, *8*, 11522.